





Structural, electrical, magnetic, and optical properties of iron-based ladder compounds $\text{BaFe}_2(\text{S}_{1-x}\text{Se}_x)_3$

Satoshi Imaizumi,¹ Takuya Aoyama ,¹ Ryota Kimura,¹ Koya Sasaki,¹ Yusuke Nambu ,² Maxim Avdeev ,^{3,4} Yasuyuki Hirata,⁵ Yuka Ikemoto,⁶ Taro Moriwaki ,⁶ Yoshinori Imai,¹ and Kenya Ohgushi¹

¹*Department of Physics, Graduate School of Science, Tohoku University, 6-3 Aramaki-Aoba, Aoba-ku, Sendai, Miyagi 980-8578, Japan*

²*Institute for Materials Research, Tohoku University, Sendai, Miyagi 980-8577, Japan*

³*Australian Nuclear Science and Technology Organisation, New Illawarra Road, Lucas Heights, New South Wales 2234, Australia*

⁴*School of Chemistry, The University of Sydney, Sydney 2006, Australia*

⁵*Department of Applied Physics, Graduate School of Science and Engineering, National Defense Academy, Hashirimizu 1-10-20 Yokosuka, Kanagawa 239-8686, Japan*

⁶*Japan Synchrotron Radiation Institute, SPring-8, Sayo, Hyogo 679-5198, Japan*



(Received 27 April 2020; revised 14 June 2020; accepted 16 June 2020; published 1 July 2020)

We performed a comprehensive study on structural, electrical, magnetic, and optical properties for iron-based ladder materials $\text{BaFe}_2(\text{S}_{1-x}\text{Se}_x)_3$ ($0 \leq x \leq 1$), which shows pressure-induced superconductivity in the vicinity of the Mott transition at $x = 0$ and 1. We obtain a complete electronic phase diagram in a temperature-composition plane, which reveals that the magnetic ground state switches from the stripe-type to the block-type phase without any intermediate phase at $x = 0.23$ with increasing x . This behavior is in sharp contrast to the filling controlled system $\text{Ba}_{1-x}\text{Cs}_x\text{Fe}_2\text{Se}_3$, in which a paramagnetic state down to the lowest temperature is realized between two magnetic ordered states. The structural transition, which is considered to be relevant to the orbital order, occurs far above the magnetic transition temperature. The magnetic and structural transition temperatures exhibit a similar composition dependence, indicating a close relationship between magnetic and orbital degrees of freedom. In addition, we found that charge dynamics are considerably influenced not only by the magnetic order but also by the structural change (orbital order) from the detailed measurements of electrical resistivity and optical conductivity spectra. We discuss the magnetism and orbital order by comparing the experimental results with the proposed theory based on the multiorbital Hubbard model. The relationship between the charge dynamics and the magnetic/orbital order is also discussed.

DOI: [10.1103/PhysRevB.102.035104](https://doi.org/10.1103/PhysRevB.102.035104)

I. INTRODUCTION

In this decade, iron-based superconductors have been actively studied as superconductors with a high superconducting transition temperature, T_c . Up to now, a large number of iron-based superconducting families have been reported; the examples include 1-1-1-1, 1-2-2, 1-1-1, 2-4-5, and 1-1 series, which respectively have a representative material of LaFeAsO , BaFe_2As_2 , LiFeAs , $\text{K}_2\text{Fe}_4\text{Se}_5$, and FeSe [1–5]. In all of these materials, the crystal structure has a square lattice of Fe atoms as a common structural motif, which is considered to be the necessary ingredient of iron-based superconductors. On the other hand, several years ago, the superconductivity was found in iron-based ladder materials BaFe_2X_3 ($X = \text{S}$ and Se), in which Fe atoms form a quasi-one-dimensional ladder lattice [6,7]. A unique aspect of these ladder materials is that the electronic state at the ambient pressure is the Mott insulating state due to the prominence of electron correlation effect in one dimension and that the superconducting phase appears in the vicinity of the metal-insulator transition (Mott transition) induced by the application of pressure. This situation is in stark contrast to two-dimensional iron-based superconductors showing a metallic behavior in all the

physical parameter space. Instead, it resembles that observed in a layered organic superconductor BEDT-TTF salt and a cation-doped fullerene superconductor $A_3@C_{60}$ ($A = \text{Cs}$ and Rb), in which the Coulomb repulsion and bandwidth with the same energy scale make the system close to the Mott transition [8–12]. Therefore, iron-based ladder materials can be regarded as an inorganic analog of organic superconductors, albeit with a crucial difference: whereas organic superconductors are well described by a single-orbital model, iron-based ladder materials possess orbital degrees of freedom. Hence, detailed investigations on the electronic properties of iron-based ladder materials are expected to give a solid foundation to fully understand how orbital degrees of freedom influence the emergence of superconductivity in strongly correlated electron systems.

There is a series of iron-based ladder materials $A\text{Fe}_2\text{X}_3$, in which crystal structure is composed of two-leg ladder units of Fe atoms formed by edge-sharing FeX_4 tetrahedra [Fig. 1(a)]. The A site accommodates monovalent and divalent ions, and the X site can accommodate chemical elements in group 16. As a consequence, 11 isomorphous compounds are known so far: KFe_2S_3 , RbFe_2S_3 , CsFe_2S_3 , TlFe_2S_3 , BaFe_2S_3 , KFe_2Se_3 , RbFe_2Se_3 , CsFe_2Se_3 , BaFe_2Se_3 , RbFe_2Te_3 , and CsFe_2Te_3

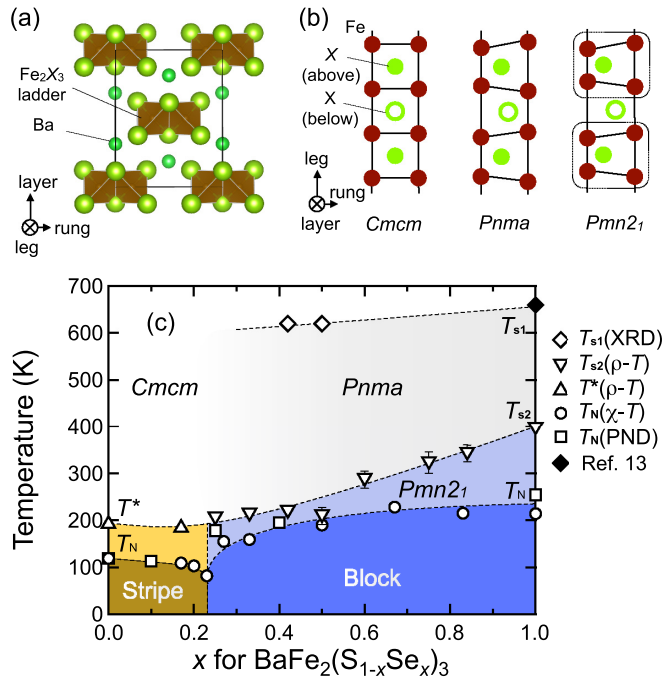


FIG. 1. (a) Crystal structure of iron-based ladder compounds BaFe_2X_3 ($X = \text{S}$ and Se). (b) Schematic pictures of the ladder structure in each orthorhombic space group, $Cmcm$, $Pnma$, and $Pmn2_1$. In $Pnma$, the rung is tilted in a staggered manner along the leg direction. In $Pmn2_1$, the tetramer structure surrounded by dotted lines, which is compatible with the block-type magnetic structure at low temperature, is formed. (c) Electronic phase diagram for $\text{BaFe}_2(\text{S}_{1-x}\text{Se}_x)_3$ obtained in this study. The structural transition temperature from $Cmcm$ to $Pnma$ at T_{s1} is determined by the high-temperature x-ray diffraction measurements (XRD). The T_{s1} value at $x = 1$ is cited from Ref. [13]. The orbital order transition temperatures at T^* and T_{s2} are estimated by the electrical resistivity (ρ) measurements. The antiferromagnetic transition temperatures (T_N) are determined by the magnetic susceptibility (χ) and powder neutron diffraction (PND) experiments. See the text for details.

[14–19]. Most of these compounds possess the orthorhombic space group $Cmcm$ in wide temperature regimes; however, special attention should be paid to Fe^{2+} -containing materials, BaFe_2S_3 and BaFe_2Se_3 . The space group of BaFe_2S_3 at room temperature is established to be the orthorhombic $Cmcm$ symmetry. On cooling, a subtle phase transition occurs at $T^* \sim 200$ K, which is due to a possible orbital order probably related to the nematic fluctuations as shown in the nematic susceptibility measurements [20,21]. However, no structural evidence has been obtained in x-ray or neutron diffraction experiments, and the crystal symmetry below T^* is unclear at present. In BaFe_2Se_3 , although the space group at room temperature had been thought to be the orthorhombic $Pnma$ symmetry, recent second-harmonic generation experiments as well as single-crystal x-ray diffraction measurements revealed the noncentrosymmetric orthorhombic $Pmn2_1$ symmetry at room temperature [22,23]. A fascinating aspect of the room-temperature phase of BaFe_2Se_3 is that the phase loses the spatial inversion symmetry, and thus the magnetically ordered phase is a multiferroic state. On warming BaFe_2Se_3 , the system transforms into the orthorhombic $Pnma$ symmetry with a

centrosymmetric symmetry at $T_{s2} = 400$ K. The driving force of this structural transition is argued in terms of the orbital ordering. On further warming BaFe_2Se_3 , the system transforms into the orthorhombic $Cmcm$ symmetry at $T_{s1} = 660$ K [13,24]. The microscopic mechanism of this structural transition at T_{s1} is unclear at present. The three orthorhombic space groups realized in BaFe_2Se_3 have a subgroup-supergroup relationship of $Cmcm \supset Pnma \supset Pmn2_1$, and there is no unit-cell discontinuous expansion/shrinkage across the transition. The schematic pictures of the ladder structure in each space group are shown in Fig. 1(b). We note that the three principal axes of the orthorhombic structure (a , b , and c) are defined in a distinct manner among three space groups; in the following, in order to avoid confusion, we take the notation to call each principal axis as the leg, rung, and layer directions (the layer direction being the direction perpendicular to both leg and rung directions).

We summarize electronic properties at ambient pressure for BaFe_2S_3 and BaFe_2Se_3 , which are targeted materials in this study. The electrical resistivity of both materials shows an insulating behavior [6,25]. This behavior is in contrast to the metallic behavior observed in the parent material of the layered iron-based superconductors with a square lattice of Fe atoms. For BaFe_2X_3 ($X = \text{S}, \text{Se}$), it can be understood as a result of a substantial electron correlation effect due to its low dimensionality, which renders the system into a Mott insulator. BaFe_2S_3 is more conductive than BaFe_2Se_3 , which is anomalous in the light of a usual chemical trend that selenides are more conductive than sulfides. This trend can be explained by smaller lattice parameters of BaFe_2S_3 in comparison with BaFe_2Se_3 . Hence, S $3p$ orbitals are more strongly hybridized with Fe $3d$ orbitals, making the bandwidth larger and the Coulomb repulsion smaller. Despite the expectation of a simple activation behavior in a Mott insulator, the resistivity exhibits a complicated temperature dependence owing to the possible orbital order. In BaFe_2S_3 , the divergence tendency becomes modest on cooling across the T^* transition. In BaFe_2Se_3 , on the other hand, the charge gap becomes larger on cooling across the T_{s2} transition. The two compounds, BaFe_2S_3 and BaFe_2Se_3 , undergo the magnetic transition at $T_N = 120$ and 255 K, respectively. The magnetic structures are actually different: the stripe-type antiferromagnetic structure with the rung direction as an easy axis in BaFe_2S_3 , and the block-type antiferromagnetic structure with the layer direction as an easy axis in BaFe_2Se_3 , which are schematically shown in Fig. 12 [6,25]. The magnetic moments at the lowest measured temperature of ~ 3 K is $1.20 \mu_B/\text{Fe}$ in BaFe_2S_3 and $2.75 \mu_B/\text{Fe}$ in BaFe_2Se_3 , which suggests that BaFe_2Se_3 is in a more strongly correlated regime than BaFe_2S_3 . The decreasing behavior of the magnetic susceptibility on cooling in the paramagnetic phase as well as the significant magnon contributions to the thermal conductance indicates the low-dimensional nature of spin dynamics in BaFe_2S_3 and BaFe_2Se_3 [26]. Actually, the spin waves revealed by inelastic neutron scattering measurements have the one-dimensional feature. The strongest magnetic exchange coupling along the leg direction is $|SJ| = 49$ meV for BaFe_2S_3 and $|SJ| = 43$ meV for BaFe_2Se_3 (S and J being the spin quantum number and the exchange interaction, respectively) [27,28]. These energy scales are much larger than the Néel

temperature. This is interpreted as the static magnetic order being suppressed by large quantum fluctuations inherent to the quasi-one-dimensional system.

When subjected to pressure, the two materials, BaFe_2S_3 and BaFe_2Se_3 , exhibit the metal-insulator transition accompanied by the superconducting transition. Among the two materials, BaFe_2S_3 has been more intimately investigated by various experimental probes. On the application of pressure to BaFe_2S_3 , the resistivity shows a monotonic decrease before showing a metallic behavior at 11.6 GPa. In the insulating phase, the magnetic transitions show a characteristic pressure dependence. With increasing pressure, T_N first increases and then shows a gradual decrease until the magnetic order disappears close to the metal-insulator transition boundary [29–31]. When entering into the metallic phase characterized by the Fermi liquid behavior, the resistivity shows a sharp drop due to the superconducting transition at low temperatures. The bulk nature of the superconductivity is confirmed by the ac magnetic susceptibility measurements. The T_c curve shows a dome-like shape in the pressure-temperature (P - T) phase diagram with a maximal superconducting temperature of $T_c = 24.6$ K [20]. In comparison to BaFe_2S_3 , less is known for BaFe_2Se_3 under pressure. The emergence of the superconductivity with $T_c = 11$ K at 11.5 GPa is reported by the resistivity measurements [7]. On the other hand, the pressure dependence of the antiferromagnetic transition temperature is determined by the neutron diffraction and the μSR experiments in the limited pressure regime [32]; the T_N values in the vicinity of the superconducting phase transitions are not yet uncovered. Moreover, the crystal structure under pressure is not fully clarified yet, and although the T_{s1} transition has been revealed to disappear above 4 GPa at room temperature, there is no information on the pressure dependence of the T_{s2} transition [24].

Since various computational techniques are applicable to the many-body Hamiltonian in one dimension, iron-based ladder materials capture significant interest from theorists. Regarding BaFe_2S_3 , first-principle calculations showed that the Fermi surface consists of two-electron surfaces and one hole surface, among which two electron surfaces are nested with each other. It is argued that this nesting stabilizes the stripe-type magnetic order and the associated spin fluctuations induce the superconductivity [33–36]. The band structure near the Fermi level is represented mostly by $3d_{xz}$ orbitals mixed with $3d_{xy}$ orbitals and $3d_{x^2-y^2}$ orbitals of Fe^{2+} ions (x , y , and z axes corresponding to the layer, rung, and leg directions of the ladder, respectively) and is well reproduced by the tight-binding model with two orbitals in the low-energy limit. Thus a constructed two-orbital Hubbard model on the ladder lattice is solved by the density matrix renormalization group method, clarifying that the experimentally observed stripe-type magnetic order is stable at half-filling as a result of competing antiferromagnetic interactions between the nearest-neighbor and the next-nearest-neighbor spins. It is also shown that doping holes into this state leads to the superconducting instability [37]. In this way, both weak- and strong-coupling theories successfully explain the magnetism and superconductivity observed in BaFe_2S_3 . Nevertheless, the microscopic mechanism of the orbital order at T^* has not yet been theoretically elucidated. Regarding BaFe_2Se_3 , on

the other hand, a five-orbital Hubbard model is constructed based on first-principles calculations. By using the Hartree-Fock approximation, it has been revealed that the block-type antiferromagnetic structure is most stable, in excellent agreement with experiments [38]. The crucial difference from BaFe_2S_3 is that BaFe_2Se_3 is the case of a more correlated regime in the Coulomb interaction U and the Hund's coupling J_H plane in comparison with BaFe_2S_3 , which is consistent with the experimentally confirmed larger magnetic moment in BaFe_2Se_3 than in BaFe_2S_3 . A structural phase transition that breaks the spatial inversion symmetry was predicted before experimental demonstrations [39]; however, the theory indicates the simultaneous occurrence of magnetic and structural transitions, which differs from the separated transitions at T_N and T_{s2} , as found experimentally [22]. The origin of superconductivity in BaFe_2Se_3 seems to not yet be fully resolved from the theoretical viewpoint.

Chemical substitution is an effective method to control electronic properties. Several substitution systems have been developed in iron-based ladder materials. Among them, $\text{Ba}_{1-x}\text{K}_x\text{Fe}_2\text{S}_3$ [40], $\text{Ba}_{1-x}\text{K}_x\text{Fe}_2\text{Se}_3$ [41], and $\text{Ba}_{1-x}\text{Cs}_x\text{Fe}_2\text{Se}_3$ [42] are categorized into the filling-controlled system, since the replacement of divalent Ba^{2+} ions by monovalent K^+ and Cs^+ ions induce carriers into the Fe $3d$ bands. In these systems, the long-range magnetic order turns out to be fragile against the carrier doping, and a paramagnetic state down to the lowest temperature of 5 K is realized. On the other hand, the recently developed solid-solution $\text{BaFe}_2(\text{S}_{1-x}\text{Se}_x)_3$ is categorized into the bandwidth-controlled system, since the replacement of S^{2-} ions and Se^{2-} ions with a distinct ionic radius induces the negative chemical pressure to the system. This solid solution is unique in a sense that the crystal/magnetic structures are distinct between two end compounds, $x = 0$ and $x = 1$. Hence, by tracking phase transitions and charge dynamics as a function of x , one can acquire valuable knowledge on the charge, spin, and orbital degrees of freedom. Up to now, the magnetic phase diagram, as well as the electrical/thermal transport properties, have been investigated for this system [26,43–45]. It was suggested from the magnetic susceptibility measurements that the ground state changes from the stripe-type order to the block-type order without any intermediate phases at $x \sim 0.20$. However, little is known on the charge dynamics and the orbital order in this system.

In this study, we synthesized single crystals of $\text{BaFe}_2(\text{S}_{1-x}\text{Se}_x)_3$ in a full composition range of x and investigated their structural, electric, magnetic, and optical properties by combining various experimental techniques including powder x-ray diffraction, electrical resistivity, reflectivity, and powder neutron diffraction experiments. As a result, we fully clarified the electronic phase diagram, which is summarized in Fig. 1(c). The phase diagram indicates a switching of the magnetic structures from the stripe-type to the block-type at $x = 0.23$, at which the orbital order pattern seems to change as well, indicating a close relationship between magnetic and orbital orders. In addition, we found that the charge dynamics are considerably influenced not only by the magnetic order but also by the orbital order, indicating the intimate coupling of the internal degrees of freedom.

II. EXPERIMENTAL

Single crystals of $\text{BaFe}_2(\text{S}_{1-x}\text{Se}_x)_3$ ($0 \leq x \leq 1$) were synthesized by the slow-cooling method [13,25,41,42]. A total amount of 1 g of the starting materials Ba, Fe, S, and Se with the molar ratio of Ba : Fe : S : Se = 1 : 2.1 : 3(1 - x) : 3x was weighed and mixed under the Ar atmosphere inside a glove box. We note that Fe is in excess of the stoichiometric ratio in order to prevent Fe vacancies in the products. The value x used in this paper is the nominal composition, which was previously shown to be achieved by appropriate synthesis [41]. The mixture was placed in a carbon crucible and sealed in an evacuated quartz tube. Then, the quartz tube was heated in a furnace. The heating sequence was varied for each composition; the temperature was raised to 1100–1150 °C for 5 h from the room temperature, held for 24 h, and then cooled down to 750 °C for 24–70 h. The crystal has a typical size of $1 \times 1 \times 5 \text{ mm}^3$ with the needle axis along the leg direction. The crystals were characterized by the powder x-ray diffraction at room temperature using Smartlab (Rigaku), with Cu $K\alpha$ radiation of the wavelength $\lambda = 1.54 \text{ \AA}$. For selected samples, powder x-ray diffraction experiments were carried out in the temperature (T) range of $T = 300\text{--}700 \text{ K}$ with temperature steps of 10 K by using SmartLab (Rigaku) with a 9-kW rotating anode. The electrical resistivity was measured by the standard four-probe dc technique with the current along the leg direction in the range of $T = 50\text{--}430 \text{ K}$.

Optical reflectivity measurements were performed using a Fourier-transform infrared spectrometer equipped with a microscope installed on the beamline BL43IR at the synchrotron radiation facility SPring-8. The incident light with a linear polarization along the leg direction was passed on the sample, and the reflected light was detected by a Si bolometer and a HgCdTe (MCT) photoconductive element in the far-infrared and mid-infrared regions, respectively. The Au plate was used as a reference. Optical conductivity spectra were obtained from the reflectivity spectra by the Kramers-Kronig transformation, in which the reflectivity spectra in the near-infrared and visible regions taken at room temperature were used as the spectra in the high-energy side. The temperature was controlled in the range of 5–300 K using a He flow cryostat.

Powder neutron diffraction data were collected on the high-resolution ECHIDNA diffractometer [46] at the Australian Nuclear Science and Technology Organisation with the neutron wavelength of $\lambda = 2.4395 \text{ \AA}$. Diffraction patterns were obtained in the temperature range $T = 4\text{--}300 \text{ K}$. The Rietveld refinements were performed using the FULLPROF suite [47]. The crystal structures were depicted by the VESTA software [48].

III. RESULTS

A. Crystal structure

We performed the powder x-ray diffraction experiments at room temperature for $\text{BaFe}_2(\text{S}_{1-x}\text{Se}_x)_3$ ($0 \leq x \leq 1$). Based on the diffraction profiles in a wide range (data not shown), we estimated the lattice parameters summarized in Fig. 2. The data obey Vegard's law. The lattice expands monotonically with increasing x , reflecting the ionic radius of Se^{2-} , which is larger than that of S^{2-} . Figure 3(a) is the x-ray diffraction

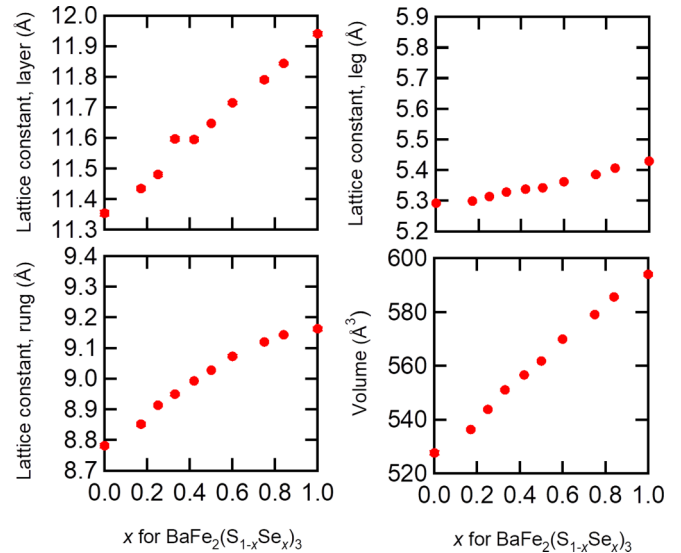


FIG. 2. Composition dependencies of lattice parameters for $\text{BaFe}_2(\text{S}_{1-x}\text{Se}_x)_3$.

profiles at room temperature focusing on the selected 2θ range including the 112 and 122 reflections; these peaks are indexed for the notation of the space group $Pmn2_1$, in which a , b , and c axes correspond to the leg, layer, and rung directions, respectively. An important point is that the 112 reflection can be allowed in the space groups $Pnma$ and $Pmn2_1$; however, it becomes forbidden in $Cmcm$ owing to the extinction rule. As seen from Fig. 3(a), the 112 reflection is not observed at $x = 0$ and 0.17, whereas it is observed at $0.25 \leq x \leq 1$. Then, we can conclude that the crystal has the $Cmcm$ symmetry with $0 \leq x \leq 0.20$ at room temperature. On the other hand, for $0.20 \leq x \leq 1$, one can say that either $Pnma$ symmetry or $Pmn2_1$ symmetry is realized from the powder x-ray diffraction measurements. By combining with the resistivity data discussed later, we conclude that the crystal symmetry is the $Pnma$ symmetry in $0.20 \leq x \leq 0.80$ and the $Pmn2_1$ symmetry in $0.80 \leq x \leq 1$ at room temperature.

Next, we carried out the powder x-ray diffraction measurements at high temperature for selected samples, $x = 0.42$ and 0.50 [Figs. 3(c) and 3(d)]. On warming up to 700 K, the 112 peaks shown by solid triangles smoothly disappear. We here note that a new peak indicated by an asterisk emerges at around $2\theta \sim 27^\circ$ at high temperature, which turned out to be originating from the unknown impurity probably generated through the oxidation process. To quantify the 112 peak intensity as a function of temperature, we estimate $I(112)/I(122)$, which is the integrated intensity ratio between the 112 peak and the fundamental 122 peak. As can be seen from Fig. 3(b), $I(112)/I(122)$ becomes negligible at $T = 500\text{--}600 \text{ K}$ for $x = 0.42$ and 0.50. Since our resistivity data presented below indicate that the structural transition between the $Pnma$ symmetry and the $Pmn2_1$ symmetry occurs below 400 K in this system, the structural transition at around 600 K is attributable to the transition between the high-temperature $Cmcm$ symmetry and the low-temperature $Pnma$ symmetry. Thus obtained T_{s1} values are plotted as a function of x in Fig. 1(c).

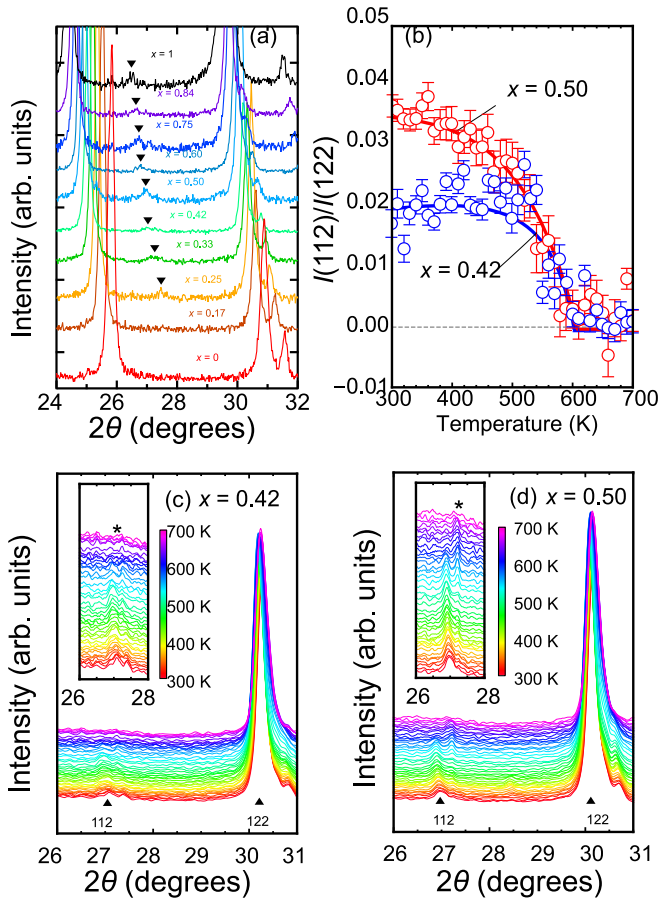


FIG. 3. Powder x-ray diffraction patterns for $\text{BaFe}_2(\text{S}_{1-x}\text{Se}_x)_3$. (a) The composition (x) dependence of x-ray diffraction profiles at room temperature. Black triangles indicate the 112 peak, which is allowed in $Pnma$ and $Pmn2_1$. (b) Temperature dependence of the 112 peak intensity scaled by the fundamental 122 peak intensity, $I(112)/I(122)$, for $x = 0.42$ and 0.50 . The error bars are standard deviations of the fitting. The solid lines are guide for eyes. (c, d) Temperature dependence of x-ray diffraction patterns focused near the 112 and 122 reflections for $x = 0.42$ (c) and 0.50 (d). Data are vertically shifted for clarity. The color bar indicates the temperature from 300 to 700 K. The inset figures are magnifications of the 122 reflection. The asterisks show the reflections from unknown impurities.

B. Electrical resistivity

Figure 4 shows the temperature dependence of the electrical resistivity with the electric current along the leg direction for $\text{BaFe}_2(\text{S}_{1-x}\text{Se}_x)_3$. All compounds investigated here are Mott insulators due to the strong-correlation effect. We estimate the activation energy Δ by fitting the data below T^* or T_{s2} with $\rho = \rho_0 \exp(\Delta/2k_B T)$, where ρ_0 is a constant value and k_B is the Boltzmann constant. As shown in the inset of Fig. 4, the activation gap becomes systematically larger with increasing x . This reflects that the replacement of S by Se acts as the negative chemical pressure effect. This can be interpreted in the following manner: since Se^{2-} ions have an ionic radius than that of S^{2-} ions, Fe $3d$ orbitals are more weakly hybridizing with Se $4p$ orbitals than with S $3p$ orbitals; this results in the smaller bandwidth and the larger

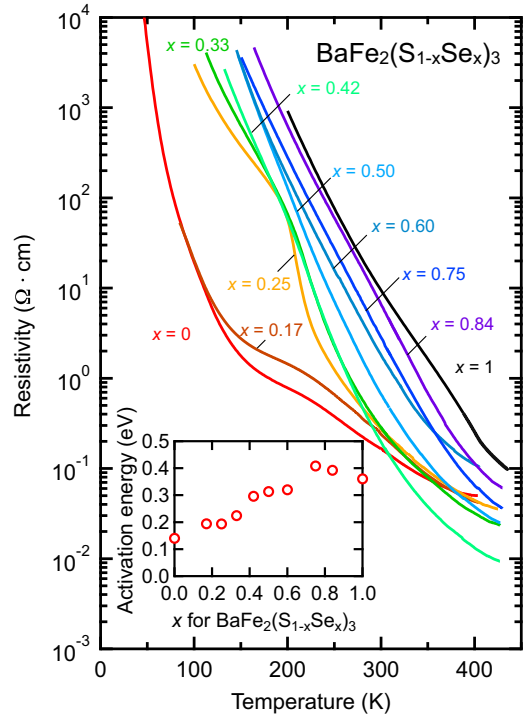


FIG. 4. Temperature dependence of the electrical resistivity (ρ) for $\text{BaFe}_2(\text{S}_{1-x}\text{Se}_x)_3$. The activation energy of each composition is shown in the inset.

Coulomb interaction in BaFe_2S_3 than in BaFe_2S_3 , leading to the observed composition dependence of the activation gap. While the resistivity apparently shows a systematic variation as a function of x , a close look at the data below 200 K reveals that this system can be separated into two groups: $0 \leq x \leq 0.20$ with the smaller resistivity and $0.20 \leq x \leq 1$ with the larger resistivity. This turns out to be related to the structural transition at T^* and T_{s2} , as discussed below.

To quantify the temperature dependence, we plot the electrical resistivity and its temperature derivative for each composition separately in Fig. 5. For $x = 0$ (BaFe_2S_3), there are two characteristic anomalies: a kink at $T_N \sim 120$ K and a change in slope at $T^* = 200$ K. The former and the latter correspond to the antiferromagnetic transition and the orbital order transition, respectively. Below T^* , the divergence tendency of ρ becomes weakened; hence, one can say that the electronic system becomes more *coherent* in the low-temperature phase. A similar behavior is also discernible at $T^* = 184$ K in $x = 0.17$.

On the other hand, there is no such signature for $0.20 \leq x \leq 1$. Instead, there is another characteristic feature, which was originally found in $x = 1$ (BaFe_2Se_3). For $x = 1$, while there is a negligible anomaly at T_N , there is a clear kink at $T_{s2} = 400$ K, at which the system undergoes the structural phase transition from the high-temperature $Pnma$ phase to the low-temperature $Pmn2_1$ phase. Below T_{s2} , the divergence tendency of ρ becomes enhanced, which is in stark contrast to the weaker divergence tendency below T^* in $0 \leq x \leq 0.20$. Hence, one can say that the electronic system becomes more *incoherent* in the low-temperature phase. The phase below T_{s2} is qualitatively distinct from the phase below T^* . The

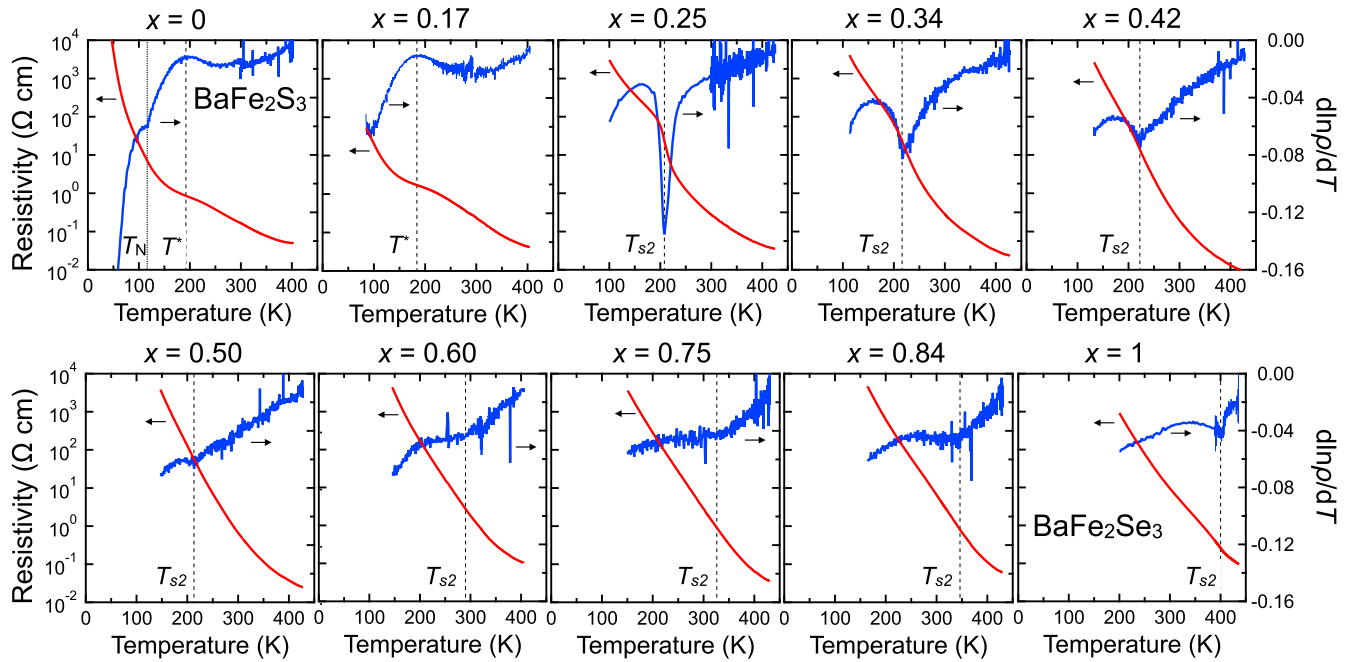


FIG. 5. Temperature (T) dependence of the electrical resistivity (ρ) and its temperature derivative $[d(\ln\rho)/dT]$ for $\text{BaFe}_2(\text{S}_{1-x}\text{Se}_x)_3$. The dotted line indicates the characteristic temperature (T^* and T_{s2}) at which an anomalous behavior caused by the structural phase transition is observed. For $x = 0$, the Néel temperature (T_N) is also shown.

T_{s2} transition is discernible in the wide composition regime, $0.20 \leq x \leq 1$. With decreasing x from $x = 1$, while the T_{s2} transition shifts to the lower temperature, the slope change across the transition becomes more prominent. This is anomalous in the sense that the presumably subtle transition in the lower T_{s2} materials has a sharper effect on ρ . The microscopic mechanism of this phenomenon is unclear at present.

The T^* and T_{s2} values estimated from the resistivity data are summarized in Fig. 1(c). In the composition range from 0.50 to 0.75, there is ambiguity in determining the exact transition temperature, which is shown as error bars in Fig. 1(c). We note that T^* and T_{s2} values show a composition dependence similar to that of T_N , indicating a close connection between the magnetic order and the orbital order.

C. Optical conductivity

Figures 6(a) and 6(b) show the reflectivity (R) and optical conductivity (σ) spectra with the light polarization along the leg direction for $\text{BaFe}_2(\text{S}_{1-x}\text{Se}_x)_3$. Here, the data taken at 5 K, which is the lowest temperature in our experiments, are shown. One can see that all compounds investigated here are Mott insulators characterized by the finite charge gap, contrasting to the metallic state characterized by the Drude components in two-dimensional iron-based superconductors. When estimating the charge gap, we have to pay attention to the fact that several optical conductivity spectra have unphysical negative values below 0.2 eV. Since these are artifacts produced in the Kramers-Kronig transformation, we hereafter consider σ with a negative value as zero. The charge gap is estimated by drawing a guideline as shown in Fig. 7, and the obtained values are plotted against x in Fig. 6(c). The monotonic enhancement of the charge gap with increasing x

is consistent with the tendency of the activation gap deduced from the electrical resistivity (inset of Fig. 4).

The absorption in this energy region is attributable to the Mott transition involving Fe 3d orbitals. Even though a Mott transition generally has broad structures with an order of a few electron volts, our experimental spectra have rather sharp peak structures with the 0.1–0.2 eV width, which is overlapping with broad absorption structures spreading over a wide energy scale of 1 eV. These are related to the multiorbital nature of the system having conduction bands with various coherence. The compounds are categorized into two groups in terms of the absorption spectrum shape: the compounds with $x = 0$ and 0.17 have absorption peaking at around 0.2 eV; the compounds with $0.25 \leq x \leq 1$ have absorption peaking at around 0.6 eV. This observation is consistent with the electrical resistivity at low temperature, i.e., the smaller resistivity in $0 \leq x \leq 0.20$ and the larger resistivity in $0.20 \leq x \leq 1$. The most important observation is that the boundary composition of two categories is very close to that of the stripe-type and block-type antiferromagnetism at low temperature: $x \sim 0.20$. This indicates that the electronic structure is strongly influenced by the magnetic order and the orbital order behind it.

We move on to the temperature dependence of the optical conductivity spectra; the data for eight selected compositions are shown in Fig. 7. For $x = 0$, as the temperature is decreased from room temperature, the spectral weight at around 0.2 eV shows anomalous evolution with a prominent peak structure at $T = 5$ K. The spectra for $x = 0.17$ show a similarly rapid growth of a peak structure at 0.2 eV on cooling. We note that these two compounds are in the stripe-type magnetic order at low temperatures. On the other hand, on cooling compounds with $0.25 \leq x \leq 1$, the spectral weight at around 0.2 eV is suppressed, and the peak structure at around 0.6 eV shows a

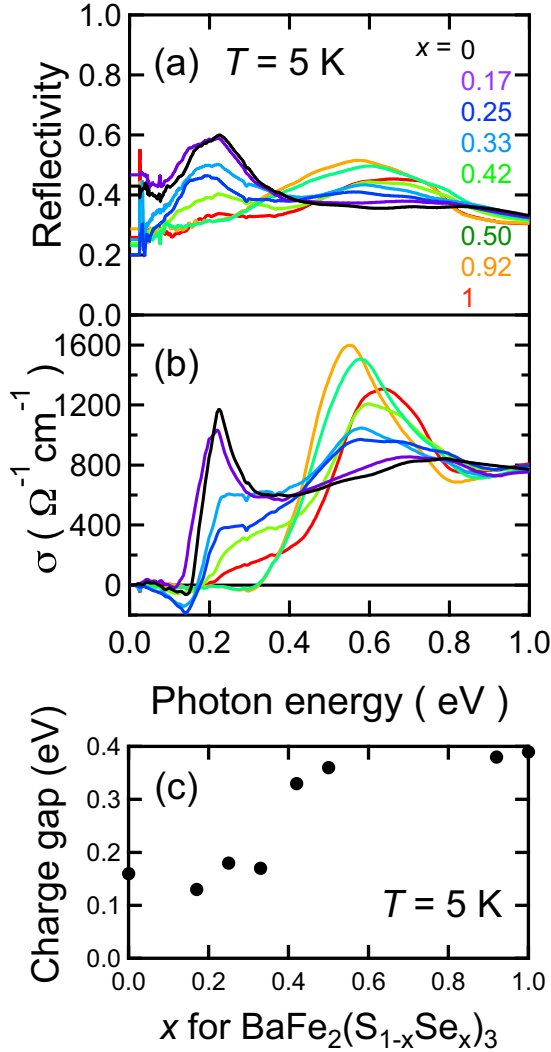


FIG. 6. (a) Optical reflectivity (R) and (b) optical conductivity (σ) spectra at the temperature (T) of 5 K for $\text{BaFe}_2(\text{S}_{1-x}\text{Se}_x)_3$. The light polarization is along the leg direction. (c) The composition dependence of the charge gap estimated from the optical conductivity spectra at 5 K for $\text{BaFe}_2(\text{S}_{1-x}\text{Se}_x)_3$.

gradual evolution. We note that these compounds are in the block-type magnetic order at low temperature.

The key finding of our reflectivity measurements is a rapid formation of a sharp peak structure centered at 0.2 eV in $0 \leq x \leq 0.20$. Such behavior is rarely observed in a Mott insulator on a three-dimensional lattice; instead, it can be frequently seen in a strongly correlated electron system in one dimension, such as organic conductors [49,50]. In a one-dimensional lattice, a formation of an antiferromagnetic order has a huge impact on the electronic structure, since a Slater insulating state is formed by a folding of the Brillouin zone. In such a system, one can expect a large temperature variation of electronic structures, particularly at the absorption edge. In order to analyze how the peak structure at 0.2 eV evolves, we calculate the effective number of carriers N_{eff} , which is a measure of the kinetic energy of carriers in a relevant energy

TABLE I. Refined crystallographic parameters of $\text{BaFe}_2(\text{S}_{1-x}\text{Se}_x)_3$ from powder neutron diffraction profiles taken at 300 K. The chemical formula unit Z is 1 for all x .

Content	$x = 0.10$	$x = 0.25$	$x = 0.40$
Molar mass (g/mol)	285.771	292.808	299.844
Space group	$Cmcm$	$Pmn2_1$	$Pmn2_1$
a (Å)	8.8348(2)	5.3148(1)	5.3307(1)
b (Å)	11.3012(2)	11.4391(2)	11.5663(3)
c (Å)	5.3007(1)	8.9148(2)	8.9855(2)
Cell volume (Å ³)	529.235	541.987	554.009
Calculated density (g/cm ³)	4.509	4.661	4.813

region,

$$N_{\text{eff}} = \frac{2m_e}{\pi e^2 N} \int_0^{\omega_c} \sigma(\omega) d\omega, \quad (1)$$

where m_e , N , and ω_c are the electron mass, the number of oscillators, and the cut-off energy, respectively. We set $\omega_c = 0.4$ eV to focus on the low-energy charge dynamics. As can be seen from Fig. 8, N_{eff} shows a contrasting temperature dependence between $0 \leq x \leq 0.20$ and $0.20 \leq x \leq 1$. For $0 \leq x \leq 0.20$, N_{eff} considerably increases on cooling, which means a spectral weight transfer from the high-energy region. The evolution of N_{eff} starts from far above T_N , hinting that the development of an orbital order at T^* plays the key role in the charge dynamics. On the other hand, for $0.20 \leq x \leq 1$, N_{eff} considerably decreases on cooling, which means the spectral weight transfers to the high-energy region. Again, in this composition range, the suppression of N_{eff} starts above T_N . One can conclude that charge dynamics in $\text{BaFe}_2(\text{S}_{1-x}\text{Se}_x)_3$ are likely influenced by the orbital order behind the magnetic order.

D. Magnetic structure

Let us move on to magnetic properties. Before describing magnetic structures, we summarize magnetic susceptibility data for $\text{BaFe}_2(\text{S}_{1-x}\text{Se}_x)_3$, which were reported elsewhere [26]. The magnetic susceptibility of all compositions shows an anomalous decrease on cooling in the paramagnetic state, which is characteristic of one-dimensional quantum magnets. Below T_N , there appears magnetic anisotropy. One can estimate T_N from the cusp in the magnetic susceptibility, which shows a nonmonotonic x dependence, as shown in Fig. 1(c). With increasing x , T_N decreases gradually from 119 K at $x = 0$ to 82 K at $x = 0.23$ and then turns to increase until it reaches 214 K at $x = 1$. The critical concentration $x \sim 0.20$ was inferred to be the transition point from the stripe-type to the block-type magnetic order.

Figure 9 shows neutron diffraction patterns at around 5 K for $\text{BaFe}_2(\text{S}_{1-x}\text{Se}_x)_3$ ($x = 0.10, 0.25$, and 0.40) together with Rietveld refinement results. Table I summarizes refined crystallographic parameters, and other crystallographic data obtained from the Rietveld refinement are shown in Table II. The determined space group is $Cmcm$ in $x = 0.10$ and $Pmn2_1$ in $x = 0.25$ and $x = 0.40$. The magnetic reflections represented by the lower green ticks of Figs. 9(a)–9(c) can be well refined by the stripe-type magnetic structure with $\mathbf{q}_m = (0.5, 0.5, 0)$ for $x = 0.10$ and the block-type magnetic structure with

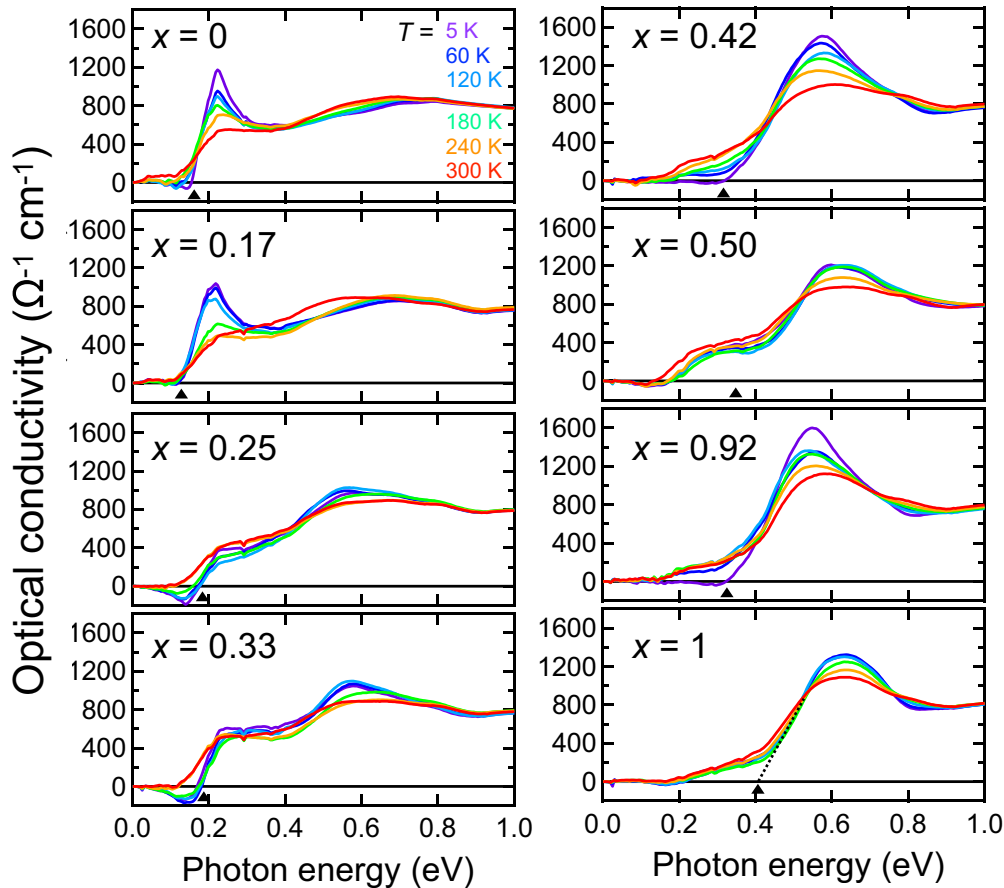


FIG. 7. Temperature (T) dependence of the optical conductivity (σ) spectra for $\text{BaFe}_2(\text{S}_{1-x}\text{Se}_x)_3$. The light polarization is along the leg direction. The dashed line and triangles are guides for estimating the charge gap.

$\mathbf{q}_m = (0.5, 0.5, 0.5)$ for $x = 0.25$ and $x = 0.40$ (\mathbf{q}_m being the magnetic propagating wave vector). Here, the hkl index is defined in the $Cmcm$ notation for $x = 0.10$ and in the $Pmn2_1$ notation for $x = 0.25$ and $x = 0.40$. The schematic pictures

of the stripe-type/block-type magnetic structures are shown in Fig. 12. For $x = 0.25$, in addition to magnetic reflections of the block-type order, weak and broad magnetic reflections corresponding to the stripe-type order were observed. This is most likely due to the coexistence of two magnetic phases near the magnetic phase boundary and is consistent with the reported results that the magnetic phase boundary exists near $x \sim 0.20$ [26,45]. In Ref. [45], the two magnetic orders were more competitive in the vicinity of the phase boundary. The realization of the same magnetic structure as in the parent compounds in the whole x regions is in stark contrast to the various magnetic structures observed in the solid solution $\text{Ba}_{1-x}\text{Cs}_x\text{Fe}_2\text{Se}_3$ [42].

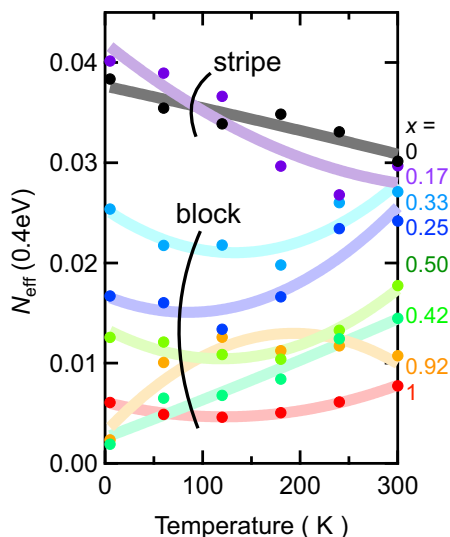


FIG. 8. The temperature dependence of the effective number of carriers (N_{eff}) in 0–0.4 eV for $\text{BaFe}_2(\text{S}_{1-x}\text{Se}_x)_3$. See the text for details.

The temperature dependencies of the diffraction patterns around the strongest magnetic reflection are shown in Figs. 9(d)–9(f). The magnetic reflections at elevated temperatures are observed at the same magnetic wave vector as the lowest temperature and are monotonically weakened toward T_N , which indicates that the magnetic transition occurs only once. Above T_N , we observe a broad peak at the same magnetic wave vector as in the magnetically ordered phase in all samples investigated here. This is due to large magnetic fluctuations inherent in the quasi-one-dimensional ladder lattice. The temperature dependence of magnetic moments estimated by the Rietveld refinement is shown in Fig. 10. The T_N value is estimated to be 113.3 ± 2.0 K in $x = 0.10$, 178.1 ± 5.9 K in $x = 0.25$, and 195.0 ± 2.7 K in $x = 0.40$ by

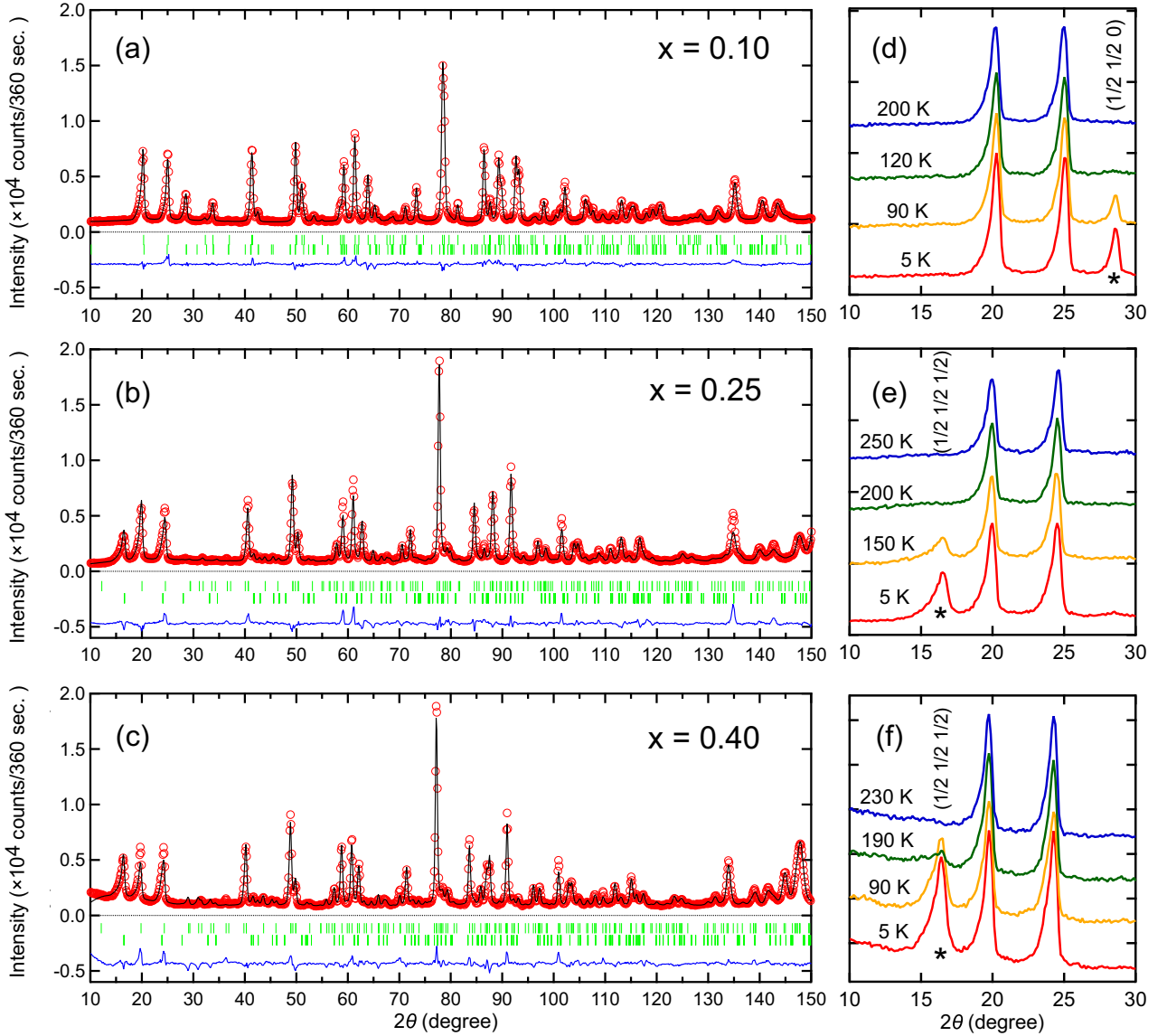


FIG. 9. High-resolution neutron powder diffraction patterns (open circles) and Rietveld refinement results (solid lines) for $\text{BaFe}_2(\text{S}_{1-x}\text{Se}_x)_3$ with the composition of (a) $x = 0.1$, (b) $x = 0.25$, and (c) $x = 0.40$. The data were taken at 5 K for $x = 0.10$ and 0.25 and at 4 K for $x = 0.40$. The space group used for the refinement is $Cmcm$ in $x = 0.1$ and $Pnm2_1$ in $x = 0.25$ and 0.40 . The calculated positions of nuclear and magnetic reflections are indicated by green ticks at upper and lower positions, respectively. The bottom blue lines give the difference between observed and calculated intensities. (d–f) Temperature evolutions of magnetic Bragg reflections for (d) $x = 0.1$, (e) $x = 0.25$, and (f) $x = 0.40$. The asterisks denote the position of magnetic reflection with $\mathbf{q}_m = (0.5, 0.5, 0)$ for $x = 0.1$ and $\mathbf{q}_m = (0.5, 0.5, 0.5)$ for $x = 0.25$ and 0.40 , where the hkl index is defined in the $Cmcm$ notation for $x = 0.10$ and the $Pnm2_1$ notation for $x = 0.25$ and 0.40 . The data were collected at the listed temperatures.

an order-parameter-type fit. The stripe magnetism is stabilized in $x = 0.10$, and the magnetic moment reaches $1.79 \mu_B$ at 4 K. The block magnetism is stabilized in $x = 0.25$ and 0.40 , and the magnetic moment reaches $2.02 \mu_B$ at 5 K for $x = 0.25$ and $2.46 \mu_B$ at 4 K for $x = 0.40$.

The magnetic moment size at the lowest temperature is plotted against the composition in the inset of Fig. 10, where the data for BaFe_2S_3 and BaFe_2Se_3 are taken from Refs. [6,25]. As x increases, the magnetic moment increases monotonically. However, a close look at the data indicates that there is a slight reduction of the magnetic moment at around $x = 0.25$ from an anticipated enhancement with increasing x .

This is possibly because the $x = 0.25$ compound locates near the magnetic phase boundary, where the XY-type anisotropy instead of Ising-like anisotropy reduces the magnetic moment through large fluctuations in spin space. Further evaluation is desired to elucidate the multicritical nature of the phase boundary.

IV. DISCUSSIONS

A. Magnetism

We now discuss the magnetism in the iron-based ladder compounds. We first recall that the increase in x corresponds

TABLE II. Refined atomic positions at 300 K for $\text{BaFe}_2(\text{S}_{1-x}\text{Se}_x)_3$. Note that the $x = 0.10$ compound takes $Cmcm$, and the $x = 0.25$ and $x = 0.40$ compounds take the $Pmn2_1$ space group. Isotropic Debye-Waller factors (U_{iso}) are employed.

Atom	Site	x	y	z	U_{iso} (\AA^2)
$x = 0.10$					
Ba	4c	1/2	0.1842(6)	1/4	0.0068(20)
Fe	8e	0.3485(3)	1/2	0	0.0071(4)
S/Se1	4c	1/2	0.6218(10)	1/4	0.0062(19)
S/Se2	8g	0.2044(8)	0.3804(7)	1/4	0.0062(19)
$x = 0.25$					
Ba1	2a	0	0.4285(23)	0.4467(43)	0.0109(31)
Ba2	2a	0	0.9402(24)	0.9850(43)	0.0109(31)
Fe1	4b	0.2482(33)	0.7397(11)	0.6085(41)	0.0083(7)
Fe2	4b	0.2504(32)	0.7538(15)	0.3079(41)	0.0083(7)
S/Se1	2a	0	0.6388(31)	0.7764(44)	0.0036(23)
S/Se2	2a	0	0.1095(23)	0.6984(50)	0.0036(23)
S/Se3	2a	0	0.8586(24)	0.4578(66)	0.0036(23)
S/Se4	2a	0	0.3883(26)	0.9300(38)	0.0036(23)
S/Se5	2a	0	0.6411(29)	0.1744(43)	0.0036(23)
S/Se6	2a	0	0.1376(26)	0.3010(54)	0.0036(23)
$x = 0.40$					
Ba1	2a	0	0.4245(20)	0.5470(29)	0.0032(28)
Ba2	2a	0	0.9450(20)	0.99285(29)	0.0032(28)
Fe1	4b	0.2511(22)	0.7597(11)	0.6843(34)	0.0104(8)
Fe2	4b	0.2479(25)	0.7447(10)	0.3847(34)	0.0104(8)
S/Se1	2a	0	0.6462(26)	0.8332(45)	0.0057(17)
S/Se2	2a	0	0.1547(26)	0.6959(45)	0.0057(17)
S/Se3	2a	0	0.8581(18)	0.5220(39)	0.0057(17)
S/Se4	2a	0	0.3957(20)	0.0639(34)	0.0057(17)
S/Se5	2a	0	0.6298(23)	0.2383(38)	0.0057(17)
S/Se6	2a	0	0.1050(21)	0.2950(38)	0.0057(17)

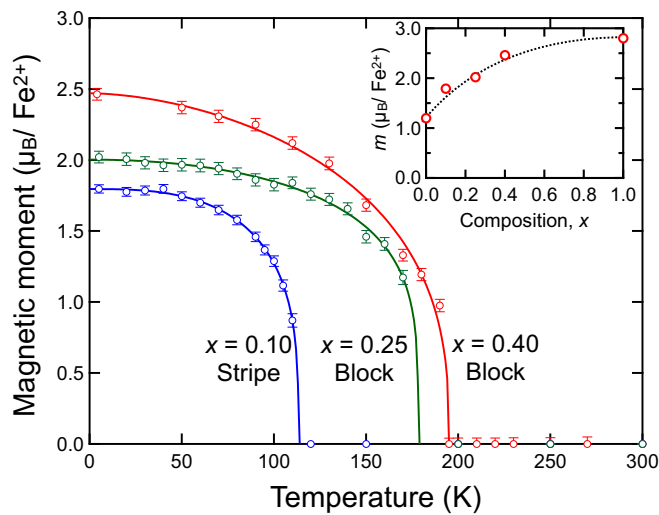


FIG. 10. Temperature dependencies of the estimated magnetic moments for $\text{BaFe}_2(\text{S}_{1-x}\text{Se}_x)_3$ with $x = 0.10$ (blue), 0.25 (green), and 0.40 (red). The inset is the composition dependence of the magnetic moment (m) at the lowest temperature around 5 K. The data for BaFe_2S_3 and BaFe_2Se_3 are taken from Refs. [6,25].

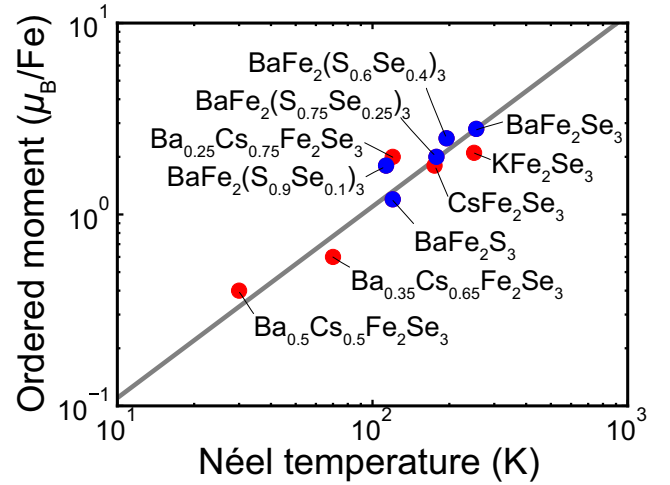


FIG. 11. The relationship between the size of the ordered magnetic moment and the Néel temperature of various iron-based ladder compounds $A\text{Fe}_2\text{X}_3$. The gray line indicates the linear relationship. The data indicated by red circles are taken from Refs. [19,42,52]. Note that the nominal Fe valence ranges from 2 to 2.5, depending on chemical compositions.

to the increase in the electron correlation effect through the narrowing of the bandwidth and the unscreened Coulomb repulsion. Our experiments indicate that, in this case, the ground state stays in the Mott insulating state with the increasing charge gap, and the magnetic structure changes from the stripe-type to the block-type magnetic order at $x = 0.23$ without any intermediate phase. The magnetic phase diagram can be well interpreted in the mean-field theory applied to the multiorbital Hubbard model proposed for iron-based ladder materials [38]; the theory revealed that the ground state changes in a series of the paramagnetic phase, the stripe-type order, the block-type order, and the ferromagnetic order with increasing U/W and J_H/W (U , W , and J_H are the on-site Coulomb interaction, the bandwidth, and the Hund's coupling, respectively). Hence, if one postulates that BaFe_2S_3 is located in a parameter space region of the stripe-type order, the block-type magnetic order in BaFe_2Se_3 is well accounted for by the theory.

Our experiments also clarified a general tendency of the enlargement of the ordered moment as well as the enhancement in T_N with increasing x . This is qualitatively consistent with a more correlated nature of BaFe_2Se_3 in comparison to BaFe_2S_3 . However, these trends could not be understood from the mean-field theory since the appearance of a full moment of $4 \mu_B$ is assumed in the theory. On the other hand, the approach of the density matrix renormalization group technique successfully explains that the ordered moment is enlarged as the electron correlation increases under the strong Hund's coupling regime [51].

To elucidate the relationship between the ordered moment and the antiferromagnetic transition temperature, we plot m against T_N for various iron-based ladder materials $A\text{Fe}_2\text{X}_3$ in Fig. 11 [19,42]. Note that we adopt a full logarithmic scale. One can see a clear linear relationship between m and T_N . This feature cannot simply be understood by the mean-field theory for the antiferromagnetic Ising model, since it leads to

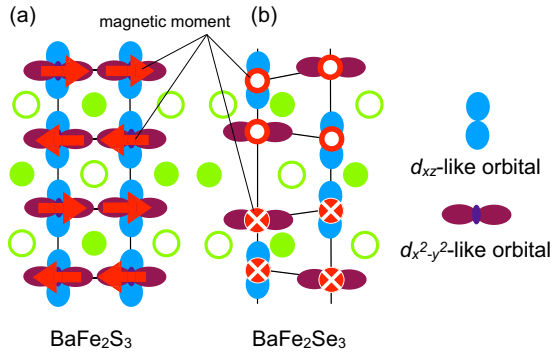


FIG. 12. The magnetic and possible orbital structures in (a) BaFe_2S_3 and (b) BaFe_2Se_3 . The anions on the upper (lower) side of the ladder layer are shown by solid (open) green circles.

$T_N \propto S(S+1) \sim m^2$ (S being the spin quantum number). This breakdown of the mean-field theory is most likely due to characteristics reflecting the one-dimensional spin system, in which magnetic fluctuations are enhanced due to the low spatial dimensionality, and the resultant antiferromagnetic transition temperature is remarkably suppressed from the nearest-neighbor exchange interaction. Another plausible reason can be a crucial role of the interlayer exchange interaction. Recent spin-wave analysis of the inelastic neutron profiles suggests that the interlayer interaction is an order of magnitude smaller than T_N in this system [27,28], and the profiles show dispersionless features along the layer stacking direction for the whole T regime measured [53], indicating large magnetic fluctuations remain even in the magnetically ordered phase.

A more complicated issue is the magnetic anisotropy. Our experiments indicate that the easy axis changes from the rung to layer directions strikingly at the composition of the magnetic transition from the stripe-type to the block-type order. The magnetic anisotropy is considered to be reasonably strong, in the light of no report on the metamagnetic transition at least up to 7 T in this system. How the spin-orbit coupling bears the magnetic anisotropy in the present system is left for a future study.

B. Crystal structure and orbital order

We next discuss structural transitions above the magnetic transition. Since the T^* transition smoothly connects with the T_{s2} transition at the critical composition of $x = 0.23$ in the electronic phase diagram [Fig. 1(c)], it is reasonable to presume that the two structural transitions have the same origin. The most plausible candidate for two transitions is the orbital order in Fe $3d$ manifolds, which is universally observed in the two-dimensional iron-based superconductors. Actually, the effective low-energy Hamiltonian deduced by the downfolding method consists of two orbitals with the d_{xz}/d_{xy} and $d_{x^2-y^2}$ characters [33]. The orbital order patterns are proposed from the experimental side. For the phase below T^* in BaFe_2S_3 , the ferroic-order of d_{xz}/d_{xy} orbitals [Fig. 12(a)] is proposed on the basis of the nematic susceptibility measurements [21]. Concerning this orbital-order pattern, whether it is cooperative or competing with the low-temperature stripe-type magnetic order is unclear at present. For the phase below T_{s2}

in BaFe_2Se_3 , the propeller-type orbital order of d_{xz}/d_{xy} and $d_{x^2-y^2}$ orbitals [Fig. 12(b)] is proposed on the basis of the second harmonic generation measurements. This orbital-order pattern is compatible with the low-temperature block-type magnetic order; hence, the orbital ordered state is considered to be driven by the magnetoelastic coupling.

Even though there is no microscopic evidence supporting the proposed orbital-order patterns for BaFe_2S_3 and BaFe_2Se_3 , these orbital-order patterns well explain the coherent/incoherent behavior of charge dynamics. One can expect that electrons are more itinerant in the ferroic-order of d_{xz}/d_{xy} orbitals below T^* , since there is no doubling of a unit cell along the leg direction in the orbital sector. This results in rather coherent charge dynamics characterized by the suppressed divergence tendency in the electrical resistivity and evolution of peak structures centered at 0.2 eV in the optical conductivity spectra below T^* . On the other hand, electrons become easily localized in the propeller-type orbital order of d_{xz}/d_{xy} and $d_{x^2-y^2}$ orbitals below T_{s2} , since the orbital ordering in a staggered manner along the leg direction results in a formation of the Slater-insulating-like state in the orbital sector. This leads to incoherent charge dynamics characterized by the enhanced charge gap below T_{s2} as observed in the electrical resistivity and optical conductivity data.

Finally, we list remaining questions on the crystal structure and orbital order in iron-based ladder materials. First, a unique aspect of this system is that the orbital and magnetic ordering temperatures differ significantly, being in stark contrast to the simultaneous occurrence in the two-dimensional iron-based superconductor BaFe_2As_2 . One possible explanation is that the orbital order is not so influenced by quantum fluctuations owing to the tight coupling with the lattice degrees of freedom with three-dimensional nature, whereas the magnetic order is easily suppressed by large quantum fluctuations in one dimension. Second, the microscopic mechanism of the T_{s1} transition is unclear at present. One possibility is that the transition is related to chemical issues such as the cation-radius mismatch. Third, how orbital ordered phases behave under pressure is open. This is quite important since the Cooper pairs in the superconducting state under high pressure can be mediated by not only spin fluctuations but also orbital fluctuations. The detailed investigations of electronic properties under high pressure in this system are left for future studies.

V. CONCLUSIONS

In this study, we performed the powder x-ray diffraction, electrical resistivity, optical reflectivity, and powder neutron diffraction experiments for single crystalline iron-based ladder compounds $\text{BaFe}_2(\text{S}_{1-x}\text{Se}_x)_3$ in a wide composition range, x . The structural and magnetic properties change dramatically at the critical concentration of $x = 0.23$: the stripe-type magnetic order and the ferroic orbital order are realized at $0 \leq x \leq 0.23$; the block-type magnetic order and the propeller-type orbital order are realized at $0.23 \leq x \leq 1$. At the composition phase boundary, the magnetic transition temperature was suppressed owing to the frustration effect of magnetic anisotropy. It was also clarified that charge dynamics characterized by the electrical resistivity and optical conductivity change continuously as a function of the

composition. However, there is a qualitative difference across the magnetic phase boundary: the fairly coherent state even in an insulating state at $0 \leq x \leq 0.23$, and the incoherent state at $0.23 \leq x \leq 1$. This feature is well explained by the difference in the proposed orbital ordering patterns between two regions.

ACKNOWLEDGMENTS

The authors gratefully acknowledge fruitful discussions with T. Yamauchi, H. Takahashi, S. Hosoi, T. Shibauchi, M. Itoh, H. Ikeda, R. Arita, and T. J. Sato. The synchrotron

radiation experiments were performed at BL43IR in SPring-8 with the approval of JASRI (Grants No. 2017A1395, No. 2017B1474, and No. 2018B1312). This work is financially supported by JSPS KAKENHI Grants No. JP19H05823, No. JP19H05822, No. JP19K21837, No. JP18H01159, No. JP16H04019, No. JP16H01062, No. JP18H04302, No. JP18K03531, No. JP16K17732, No. JP20K14396, No. JP17H05474, No. JP19H04685, No. JP19H04683, No. JP17H06137, and No. JP16H04007 and by the Murata Science Foundation. This work was also supported by JST CREST Grant No. JP19198318, Japan.

-
- [1] Y. Kamihara, T. Watanabe, M. Hirano, and H. Hosono, *J. Am. Chem. Soc.* **130**, 3296 (2008).
- [2] J. Paglione and R. L. Greene, *Nat. Phys.* **6**, 645 (2010).
- [3] G. R. Stewart, *Rev. Mod. Phys.* **83**, 1589 (2011).
- [4] P. Dai, J. Hu, and E. Dagotto, *Nat. Phys.* **8**, 709 (2012).
- [5] E. Dagotto, *Rev. Mod. Phys.* **85**, 849 (2013).
- [6] H. Takahashi, A. Sugimoto, Y. Nambu, T. Yamauchi, Y. Hirata, T. Kawakami, M. Avdeev, K. Matsubayashi, F. Du, C. Kawashima, H. Soeda, S. Nakano, Y. Uwatoko, Y. Ueda, T. J. Sato, and K. Ohgushi, *Nat. Mater.* **14**, 1008 (2015).
- [7] J. Ying, H. Lei, C. Petrovic, Y. Xiao, and V. V. Struzhkin, *Phys. Rev. B* **95**, 241109(R) (2017).
- [8] S. Lefebvre, P. Wzietek, S. Brown, C. Bourbonnais, D. Jérôme, C. Mézière, M. Fourmigué, and P. Batail, *Phys. Rev. Lett.* **85**, 5420 (2000).
- [9] F. Kagawa, T. Ito, K. Miyagawa, and K. Kanoda, *Phys. Rev. B* **69**, 064511 (2004).
- [10] Y. Kurosaki, Y. Shimizu, K. Miyagawa, K. Kanoda, and G. Saito, *Phys. Rev. Lett.* **95**, 177001 (2005).
- [11] A. Y. Ganin, Y. Takabayashi, Y. Z. Khimyak, S. Margadonna, A. Tamai, M. J. Rosseinsky, and K. Prassides, *Nat. Mater.* **7**, 367 (2008).
- [12] Y. Takabayashi, A. Y. Ganin, P. Jeglic, D. Arcon, T. Takano, Y. Iwasa, Y. Ohishi, M. Takata, N. Takeshita, K. Prassides, and M. J. Rosseinsky, *Science* **323**, 1585 (2009).
- [13] V. Svitlyk, D. Chernyshov, E. Pomjakushina, A. Krzton-Maziopa, K. Conder, V. Pomjakushin, R. Pöttgen, and V. Dmitriev, *J. Phys.: Condens. Matter* **25**, 315403 (2013).
- [14] K. O. Klepp, W. Sparlinek, and H. Boller, *J. Alloys Compd.* **238**, 1 (1996).
- [15] H. Y. Hong and H. Steinfink, *J. Solid State Chem.* **5**, 93 (1972).
- [16] T. Balić-Žunić, L. Karanović, and D. Poleti, *Acta Chim. Slov.* **55**, 801 (2008).
- [17] G. Amthauer and K. Bente, *Naturwissenschaften* **70**, 146 (1983).
- [18] R. H. Mitchell, K. C. Ross, and E. G. Potter, *J. Solid State Chem.* **177**, 1867 (2004).
- [19] J. M. Caron, J. R. Neilson, D. C. Miller, K. Arpino, A. Llobet, and T. M. McQueen, *Phys. Rev. B* **85**, 180405(R) (2012).
- [20] T. Yamauchi, Y. Hirata, Y. Ueda, and K. Ohgushi, *Phys. Rev. Lett.* **115**, 246402 (2015).
- [21] S. Hosoi, T. Aoyama, K. Ishida, Y. Mizukami, K. Hashizume, S. Imaizumi, Y. Imai, Ohgushi, Y. Nambu, M. Kimata, S. Kimura, and T. Shibauchi (unpublished).
- [22] T. Aoyama, S. Imaizumi, T. Togashi, Y. Sato, K. Hashizume, Y. Nambu, Y. Hirata, M. Matsubara, and K. Ohgushi, *Phys. Rev. B* **99**, 241109(R) (2019).
- [23] W. Zheng, V. Balédent, M. B. Lepetit, P. Retailleau, E. V. Elslande, C. R. Pasquier, P. Auban-Senzier, A. Forget, D. Colson, and P. Foury-Leykian, *Phys. Rev. B* **101**, 020101(R) (2020).
- [24] V. Svitlyk, G. Garbarino, A. D. Rosa, E. Pomjakushina, A. Krzton-Maziopa, K. Conder, M. Nunez-Regueiro, and M. Mezouar, *J. Phys.: Condens. Matter* **31**, 085401 (2019).
- [25] Y. Nambu, K. Ohgushi, S. Suzuki, F. Du, M. Avdeev, Y. Uwatoko, K. Munakata, H. Fukazawa, S. Chi, Y. Ueda, and T. J. Sato, *Phys. Rev. B* **85**, 064413 (2012).
- [26] F. Du, Y. Ueda, and K. Ohgushi, *Phys. Rev. Lett.* **123**, 086601 (2019).
- [27] M. Mourigal, S. Wu, M. B. Stone, J. R. Neilson, J. M. Caron, T. M. McQueen, and C. L. Broholm, *Phys. Rev. Lett.* **115**, 047401 (2015).
- [28] M. Wang, S. J. Jin, M. Yi, Y. Song, H. C. Jiang, W. L. Zhang, H. L. Sun, H. Q. Luo, A. D. Christianson, E. Bourret-Courchesne, D. H. Lee, D. X. Yao, and R. J. Birgeneau, *Phys. Rev. B* **95**, 060502(R) (2017).
- [29] S. Chi, Y. Uwatoko, H. Cao, Y. Hirata, K. Hashizume, T. Aoyama, and K. Ohgushi, *Phys. Rev. Lett.* **117**, 047003 (2016).
- [30] L. Zheng, B. A. Frandsen, C. Wu, M. Yi, S. Wu, Q. Huang, E. Bourret-Courchesne, G. Simutis, R. Khasanov, D. X. Yao, M. Wang, and R. J. Birgeneau, *Phys. Rev. B* **98**, 180402(R) (2018).
- [31] P. Materne, W. Bi, J. Zhao, M. Y. Hu, M. L. Amigó, S. Seiro, S. Aswartham, B. Büchner, and E. E. Alp, *Phys. Rev. B* **99**, 020505(R) (2019).
- [32] S. Wu, J. Yin, T. Smart, A. Acharya, C. L. Bull, N. P. Funnell, T. R. Forrest, G. Simutis, R. Khasanov, S. K. Lewin, M. Wang, B. A. Frandsen, R. Jeanloz, and R. J. Birgeneau, *Phys. Rev. B* **100**, 214511 (2019).
- [33] R. Arita, H. Ikeda, S. Sakai, and M.-T. Suzuki, *Phys. Rev. B* **92**, 054515 (2015).
- [34] M.-T. Suzuki, R. Arita, and H. Ikeda, *Phys. Rev. B* **92**, 085116 (2015).
- [35] Y. Zhang, L. Lin, J. J. Zhang, E. Dagotto, and S. Dong, *Phys. Rev. B* **95**, 115154 (2017).
- [36] L. Craco and S. Leoni, *Phys. Rev. B* **98**, 195107 (2018).
- [37] N. D. Patel, A. Nocera, G. Alvarez, R. Arita, A. Moreo, and E. Dagotto, *Phys. Rev. B* **94**, 075119 (2016).

- [38] Q. Luo, A. Nicholson, J. Rincón, S. Liang, J. Riera, G. Alvarez, L. Wang, W. Ku, G. D. Samolyuk, A. Moreo, and E. Dagotto, *Phys. Rev. B* **87**, 024404 (2013).
- [39] S. Dong, J. M. Liu, and E. Dagotto, *Phys. Rev. Lett.* **113**, 187204 (2014).
- [40] J. M. Caron, J. R. Neilson, D. C. Miller, A. Llobet, and T. M. McQueen, *Phys. Rev. B* **84**, 180409(R) (2011).
- [41] Y. Hirata, S. Maki, J. I. Yamaura, T. Yamauchi, and K. Ohgushi, *Phys. Rev. B* **92**, 205109 (2015).
- [42] T. Hawai, Y. Nambu, K. Ohgushi, F. Du, Y. Hirata, M. Avdeev, Y. Uwatoko, Y. Sekine, H. Fukazawa, J. Ma, S. Chi, Y. Ueda, H. Yoshizawa, and T. J. Sato, *Phys. Rev. B* **91**, 184416 (2015).
- [43] S. Wu, B. A. Frandsen, M. Wang, M. Yi, and R. Birgeneau, *J. Supercond. Novel Magn.* **33**, 143 (2020).
- [44] H. Sun, X. Li, Y. Zhou, J. Yu, B. A. Frandsen, S. Wu, Z. Xu, S. Jiang, Q. Huang, E. Bourret-Courchesne, L. Sun, J. W. Lynn, R. J. Birgeneau, and M. Wang, *Phys. Rev. B* **101**, 205129 (2020).
- [45] J. Yu, M. Wang, B. A. Frandsen, H. Sun, J. Yin, Z. Liu, S. Wu, and M. Yi, [arXiv:2004.06426](https://arxiv.org/abs/2004.06426).
- [46] M. Avdeev and J. R. Hester, *J. Appl. Crystallogr.* **51**, 1597 (2018).
- [47] J. Rodriguez-Carvajal, *Phys. B (Amsterdam, Neth.)* **192**, 55 (1993).
- [48] K. Momma and F. Izumi, *J. Appl. Crystallogr.* **44**, 1272 (2011).
- [49] D. Controzzi, F. H. L. Essler, and A. M. Tsvelik, *Phys. Rev. Lett.* **86**, 680 (2001).
- [50] M. Mitrano, G. Cotugno, S. R. Clark, R. Singla, S. Kaiser, J. Stähler, R. Beyer, M. Dressel, L. Baldassarre, D. Nicoletti, A. Perucchi, T. Hasegawa, H. Okamoto, D. Jaksch, and A. Cavalleri, *Phys. Rev. Lett.* **112**, 117801 (2014).
- [51] J. Rincón, A. Moreo, G. Alvarez, and E. Dagotto, *Phys. Rev. Lett.* **112**, 106405 (2014).
- [52] M. Wang, M. Yi, S. Jin, H. Jiang, Y. Song, H. Luo, A. D. Christianson, C. de La Cruz, E. Bourret-Courchesne, D. X. Yao, D. H. Lee, and R. J. Birgeneau, *Phys. Rev. B* **94**, 041111(R) (2016).
- [53] T. Hawai (private communication).